BIOPHYSICS AND BASIC BIOMEDICAL RESEARCH – Full Paper

Magnetic Resonance in Medicine 65:1448–1460 (2011)

Spin-Locking Versus Chemical Exchange Saturation Transfer MRI for Investigating Chemical Exchange Process Between Water and Labile Metabolite Protons

Tao Jin,[1]* Joonas Autio,[2,3] Takayuki Obata,[2] and Seong-Gi Kim[1,4]

Chemical exchange saturation transfer (CEST) and spin-locking (SL) experiments were both able to probe the exchange process between protons of nonequivalent chemical environments. To compare the characteristics of the CEST and SL approaches in the study of chemical exchange effects, we performed CEST and SL experiments at varied pH and concentrated metabolite phantoms with exchangeable amide, amine, and hydroxyl protons at 9.4 T. Our results show that: (i) on-resonance SL is most sensitive to chemical exchanges in the intermediate-exchange regime and is able to detect hydroxyl and amine protons on a millimolar concentration scale. Off-resonance SL and CEST approaches are sensitive to slow-exchanging protons when an optimal SL or saturation pulse power matches the exchanging rate, respectively. (ii) Offset frequency-dependent SL and CEST spectra are very similar and can be explained well with an SL model recently developed by Trott and Palmer (J Magn Reson 2002;154:157–160). (iii) The exchange rate and population of metabolite protons can be determined from offset-dependent SL or CEST spectra or from on-resonance SL relaxation dispersion measurements. (iv) The asymmetry of the magnetization transfer ratio (MTR_{asym}) is highly dependent on the choice of saturation pulse power. In the intermediate-exchange regime, MTR_{asym} becomes complicated and should be interpreted with care. Magn Reson Med 65:1448–1460, 2011. ©2010 Wiley-Liss, Inc.

Key words: chemical exchange; spin locking; CEST; asymmetric population approximation; MTR asymmetry

Recently, there has been an increasing number of in vivo studies that have used the chemical exchange (CE) effect to probe the tissue microenvironment and provide novel imaging contrasts that are not available from conventional MRI techniques. Most of these studies adopted either a chemical exchange saturation transfer (CEST) or a spin-locking (SL) approach to detect contrast in tissue pH or the population of labile protons, which have a Larmor frequency different from water. Ideally, a CE-sensitive imaging contrast should have good sensitivity and vary monotonically with pH and linearly with labile proton concentration. The CE contrast is determined by many parameters, such as the exchange rate between water and labile protons (k_{ex}), the difference in their Larmor frequencies (δ), the populations of the exchangeable protons, water T_1, and the magnetic field strength (B_0). The CE effect in MRI is also highly sensitive to a ratio of k_{ex} to δ. k_{ex}/δ, which indicates the CE kinetics, is usually divided into three regimes: slow ($k_{ex}/\delta \ll 1$), intermediate ($k_{ex}/\delta \sim 1$), and fast exchange ($k_{ex}/\delta \gg 1$). CEST techniques are mostly applied at the slow- or slow- to intermediate-exchange regime (1,2), whileas the CE is often assumed to occur at the fast-exchange regime for SL applications (3,4).

In CEST studies that are based upon endogenous contrast, selective off-resonance irradiation of labile protons of protein or peptide side chains attenuates the water signal via exchange between these labile protons and bulk water. The signal intensity as a function of irradiation frequency, often referred to as the Z-spectrum, can be expressed by the magnetization transfer ratio (MTR):

$$\mathrm{MTR}(\Omega) = {}^{M_{\mathrm{CEST}}(\Omega)}/_{M_0}, \qquad [1]$$

where Ω is the frequency offset with respect to water. In practice, the conventional non-CE magnetization transfer effect and direct water saturation (or the so-called spill-over effect) also affect the Z-spectrum, and these effects are assumed to be symmetrical around the water resonance frequency. To minimize these non-CE contributions, CEST contrast in MRI is usually extracted from two images—one acquired with off-resonance irradiation on the targeted labile proton and the other as a control with opposite offset frequency from the water (5). The normalized differential image, usually referred to as the asymmetry of MTR (MTR_{asym}), is described as

$$\mathrm{MTR}_{\mathrm{asym}}(\Omega) = \mathrm{MTR}(-\Omega) - \mathrm{MTR}(\Omega), \qquad [2]$$

which is sensitive to the CE effect. Previous endogenous CEST contrast is mostly based on protons in slow-exchanging regimes and has been applied in many pathological studies. For example, the amide proton transfer approach, which is based upon the exchange between amide protons of protein side chains and water, has been used to study tumor or stroke (5–7). At neutral pH, amide protons typically have a chemical shift of around 3.5 ppm (1400 Hz or 8800 rad/sec at 9.4 T) from water, and

[1]Department of Radiology, University of Pittsburgh, Pittsburgh, Pennsylvania, USA.

[2]Department of Biophysics, Molecular Imaging Center, National Institute of Radiological Sciences, Chiba, Japan.

[3]Department of Neurobiology, A. I. Virtanen–Institute, University of Kuopio, Kuopio, Finland.

[4]Department of Neurobiology, University of Pittsburgh, Pittsburgh, Pennsylvania, USA.

Grant sponsor: NIH; Grant numbers: EB008717, EB003324, EB003375, NS44589.

*Correspondence to: Tao Jin, Ph.D., Department of Radiology, University of Pittsburgh, 3025 E Carson Street, Room 156, Pittsburgh, PA 15203.
E-mail: taj6@pitt.edu

Received 3 August 2010; revised 13 October 2010; accepted 17 October 2010.

DOI 10.1002/mrm.22721
Published online 30 November 2010 in Wiley Online Library (wileyonlinelibrary.com).

the exchange rate with water proton is on the order of 100 sec^{-1} (8). Recently, endogenous CEST contrast has also been observed on faster exchanging protons, where, for example, hydroxyl-based CEST approaches were reported to provide information on the concentration of glycogen and glycosaminoglycans (9,10). These hydroxyl protons have chemical shifts of 1–3 ppm from water and exchange rates on the order of 700–15,000 sec^{-1} (1,8); thus, the exchange is close to the intermediate regime for 3 T (1 ppm = 128 Hz or 802 rad/sec) or even 9.4 T.

The CE effect can also be studied by an SL approach, where water magnetization is first flipped away from the *Z*-axis and then spin locked by either an on- or off-resonance B_1 radiofrequency pulse. During the applied SL pulse, the water magnetization decays with the spin-lattice relaxation time in the rotating frame ($T_{1\rho}$), which is sensitive to molecular fluctations with a frequency that is close to the Rabi frequency of the SL pulse, $\omega_{1,\,SL}$ ($=\gamma B_{1,\,SL}$). SL contrast has been used to characterize cartilage degradation (11–13), tumors (14–17), stroke (18,19), and neurodegenerative diseases (20,21). The $T_{1\rho}$ dependence on $\omega_{1,\,SL}$, referred to as the $T_{1\rho}$ dispersion, has also been applied in pathological studies (16,19,22). It was reported in protein phantoms that the CE effect contributes significantly to the $T_{1\rho}$ dispersion in the $\omega_{1,\,SL}$ range below a few kilohertz (11,23). Previous SL studies of CE effects were often explained by theoretical models with fast-exchange approximation (3,4). This assumption has hindered the application of SL approaches to slow- and intermediate-exchange protons, which are widely present in biological tissues. Recently, Trott and Palmer proposed a theoretical description to explain the CE contribution to the relaxation rate $R_{1\rho}$ ($=1/T_{1\rho}$) when the populations of two exchanging proton pools are highly unequal (24). Under such asymmetric population (AP) approximation, the expression of CE contribution to $R_{1\rho}$ can be simplified and applied beyond the fast-exchange limit (24). The AP assumption holds for most in vivo CE applications, because water is the dominant pool; thus, the Trott and Palmer model may be applicable to in vivo SL studies.

The aims of this work are as follows: (i) to examine the characteristics of SL and CEST contrast for CEs in the slow-, intemediate-, and fast-exchange regimes, and (ii) to explain experimental data with Trott and Palmer's AP model. On-resonance $R_{1\rho}$ dispersion, offset-dependent SL spectra, and CEST *Z*-spectra measurements were performed at varied pH and concentrated metabolite phantoms with typical exchangeable proton groups found in vivo, including amide, hydroxyl, and amine protons.

THEORETICAL BACKGROUNDS

The pulse sequence for an SL experiment is illustrated in Fig. 1a, where the superscripts and subscripts of a radiofrequency pulse denote its phase and transmitter frequency, respectively. The SL pulse has a Rabi frequency (SL frequency) $\omega_{1,\,SL}$ and is applied on the *Y*-axis at a frequency offset Ω; thus, in the rotating frame, the effective SL field $B_{1,\mathrm{eff}} = \sqrt{\omega_{1,\mathrm{SL}}^2 + \Omega^2}/\gamma$ (Fig. 1b). To achieve SL, the water magnetization is first flipped by the θ degree pulse to the *Y*–*Z* plane, then spin locked by $B_{1,\,\mathrm{eff}}$ for duration of spin-locking time (TSL), and then flipped back to the *Z*-axis for imaging. During TSL, the water magnetization is locked at an angle $\theta = \arctan(\omega_{1,\mathrm{SL}} / \Omega)$ from the *Z*-axis and decays with $R_{1\rho}$, the spin-lattice relaxation rate in the rotating frame (Fig. 1c). Provided that the spin relaxation is dominated by single-exponential decay, $R_{1\rho}$ can generally be expressed as:

$$R_{1\rho} = R_1 \cdot \cos^2\theta + (R_2 + R_{\mathrm{ex}}) \cdot \sin^2\theta, \qquad [3]$$

where R_1 is the longitudinal relaxation rate of water and R_2 is the intrinsic water transverse relaxation rate in the absence of CE. A special case is when $\Omega = 0$ and $\theta = 90^\circ$, which is the on-resonance SL. For two-site exchange between A and B with different magnetic environments (representing water and labile nonwater protons, respectively), the population (p) of each site and the exchange rate constant (k) satisfy $p_A\, k_A = p_B\, k_B$. Using population-averaged values of R_1 and R_2 for protons in the two sites and assuming that the populations of the two sites are highly asymmetric ($p_A \gg p_B$), the Bloch–McConnell equation can be solved, and the CE-related relaxation rate in an SL experiment, with Ω and $\omega_{1,\,SL}$ as experimental variables, can be written as (24)

$$R_{\mathrm{ex}}(\Omega, \omega_{1,\mathrm{SL}}) = \frac{p_B \cdot \delta^2 \cdot k_{\mathrm{ex}}}{(\delta - \Omega)^2 + \omega_{1,\mathrm{SL}}^2 + k_{\mathrm{ex}}^2}, \qquad [4]$$

where δ is the chemical shift of the labile proton relative to water, $k_{ex} = k_A + k_B$ is the exchange rate between the two proton pools, and $p_A \approx 1$ is assumed. Note that the frequency offset is expressed relative to the Larmor frequency of water, and some notations are different from those in the original reference of Trott and Palmer (Ω and k_{ex} correspond to ω_{rf} and k, respectively). R_{ex} reaches a peak at $\Omega = \delta$. The parameters of interest, p_B, k_{ex}, and δ, can be obtained by fitting R_{ex} with Eq. 4. To this end, two SL approaches are adopted; change in $\omega_{1,SL}$ with fixed Ω and change in Ω with fixed $\omega_{1,SL}$.

SL measurements as a function of $\omega_{1,SL}$ can be performed at $\Omega = 0$ (on-resonance SL) or $\Omega = \delta$. For on-resonance SL ($\Omega = 0$),

$$R_{\mathrm{ex}}(\omega_{1,\mathrm{SL}}) = \frac{p_B \cdot k_{\mathrm{ex}}}{1 + (\omega_{1,\mathrm{SL}}/\delta)^2 + (k_{\mathrm{ex}}/\delta)^2}. \qquad [5]$$

The SL relaxation rate is

$$R_{1\rho} = R_2 + R_{\mathrm{ex}} = R_2 + \frac{p_B \cdot k_{\mathrm{ex}}}{1 + (\omega_{1,\mathrm{SL}}/\delta)^2 + (k_{\mathrm{ex}}/\delta)^2}. \qquad [6]$$

The on-resonance $R_{1\rho}$ dispersion data can be fitted to $\omega_{1,\,SL}$ to obtain p_B and k_{ex} in addition to R_2 and δ. If δ is known, k_{ex} can also be inferred from the linewidth of the $R_{ex}(\omega_{1,\,SL})$ Lorentzian-shaped curve (R_{ex} vs. $\omega_{1,\,SL}$ plot): full width at half maximum (FWHM) $= \sqrt{k_{ex}^2 + \delta^2}$. In the case of $k_{ex}/\delta_B \ll 1$, however, p_B and k_{ex} cannot be separately determined from on-resonance $R_{1\rho}$ dispersion. Another SL offset frequency of particular interest is the Larmor frequency of the labile proton B ($\Omega = \delta$), for which

$$R_{\mathrm{ex}}(\omega_{1,\mathrm{SL}}) = \frac{p_B \cdot k_{\mathrm{ex}}}{(\omega_{1,\mathrm{SL}}/\delta)^2 + (k_{\mathrm{ex}}/\delta)^2} \qquad [7]$$

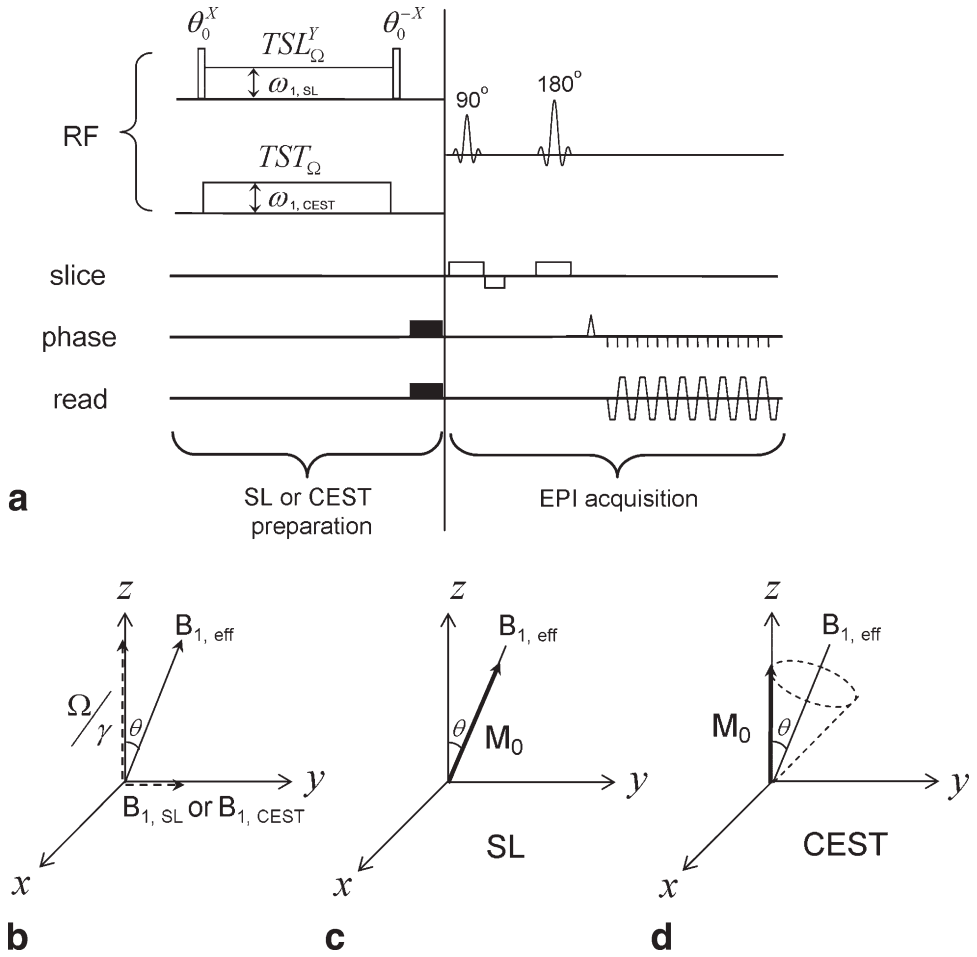

FIG. 1. **a**: The pulse sequence diagram used for the SL and CEST experiments contains an SL or CEST preparation pulse and a spin-echo echo-planar imaging acquisition. The superscripts and subscripts of a radiofrequency pulse denote its phase and transmitter frequency, respectively. For SL, the water magnetization is first flipped by a hard pulse and then locked by an SL pulse with a Rabi frequency of $\omega_{1,\,SL}$ ($=\gamma B_{1,\,SL}$) and a duration of TSL. The hard pulse following the SL pulse flips the magnetization back to the *Z*-axis. For CEST, the saturation pulse has a Rabi frequency of $\omega_{1,\,CEST}$ and a duration of TST (saturation time). **b**: With an off-resonance $B_{1,\,SL}$ or $B_{1,\,CEST}$ pulse applied at the frequency offset Ω, the water magnetization in the rotating frame experiences an effective $B_{1,\,eff}$ that has an angle θ with the *Z*-axis. **c**: In an SL experiment, the water magnetization M_0 was flipped to the $B_{1,\,eff}$ direction and was spin locked by $B_{1,\,eff}$. **d**: In a CEST experiment, the magnetization precesses around $B_{1,\,eff}$.

SL experiments can also be performed as a function of offset frequency (Ω) with a fixed $\omega_{1,\,SL}$, similar to a CEST *Z*-spectrum. The magnetization at a TSL, with repetition time $\rightarrow \infty$, is

$$\frac{M(\Omega)}{M_0}=\frac{(R_2+R_{ex})\sin^2\theta\cdot\exp\{-[(R_2+R_{ex})\sin^2\theta+R_1\cos^2\theta]\cdot \mathrm{TSL}\}+R_1\cos^2\theta}{(R_2+R_{ex})\sin^2\theta+R_1\cos^2\theta}, \quad [8]$$

When TSL is sufficiently long, the magnetization reaches steady state. An SL ratio (SLR) can be described, similar to MTR of CEST studies (see Eq. 1), as

$$\mathrm{SLR}(\Omega)=\frac{M_{SL}(\Omega)}{M_0}=\frac{R_1\cos^2\theta}{(R_2+R_{ex})\sin^2\theta+R_1\cos^2\theta}, \quad [9]$$

Ω-dependent SLR spectrum will be referred to as the SL *Z*-spectrum for comparison with the CEST *Z*-spectrum. Similar to $\mathrm{MTR_{asym}}$ (see Eq. 2), the CE-related contrast can be obtained from the asymmetry of the SLR; i.e., the normalized differential signal acquired from opposite frequency offsets with respect to water:

$$\mathrm{SLR_{asym}}(\Omega)=\mathrm{SLR}(-\Omega)-\mathrm{SLR}(\Omega) \quad [10]$$

In off-resonance SL studies with varying Ω, R_{ex} can be obtained by rearranging Eq. 9 from an SL *Z*-spectrum:

$$R_{ex}(\Omega)=(1/\mathrm{SLR}-1)\cdot\frac{\Omega^2}{\omega_{1,SL}^2}\cdot R_1-R_2. \quad [11]$$

Ω-dependent R_{ex} can be used for fitting k_{ex} and p_B from Eq. 4. The exchange rate k_{ex} can also be inferred from the linewidth of the R_{ex} Lorentzian-shaped curve (R_{ex} vs. Ω plot): FWHM $=\sqrt{k_{ex}^2+\omega_{1,SL}^2}$. To compare

CEST results with the SL approach, an effective $R_{ex,\ CEST}$ may be constructed from the CEST *Z*-spectra, similar to Eq. 11:

$$R_{ex,CEST}(\Omega) = (1/MTR - 1) \cdot \frac{\Omega^2}{\omega_{1,CEST}^2} \cdot R_1 - R_2 \qquad [12]$$

If $R_{ex,\ CEST}(\Omega)$ is similar to $R_{ex}(\Omega)$ (at $\omega_{1,\ CEST} = \omega_{1,\ SL}$), k_{ex} can be inferred from FWHM of the $R_{ex,\ CEST}$ vs. Ω plot and also determined using Eq. 4.

MATERIALS AND METHODS

MR Experiments of Metabolite Phantoms

All MR experiments were performed at room temperature on a 9.4 T/31-cm magnet (Magnex, UK), interfaced to a Unity INOVA console (Varian). The actively shielded 12-cm-diameter gradient insert (Magnex, UK) operates at a maximum gradient strength of 40 gauss/cm and a rise time of 120 μsec. A 3.8-cm-diameter volume coil (Rapid Biomedical, OH) was used for excitation and reception. Metabolite solution (see below) was transferred into a 9-mm I.D. syringe, and three or four syringes were inserted together into the coil for imaging. Magnetic field homogeneity was optimized by localized shimming over a $\sim 20 \times 20 \times 6$ mm^3 volume to yield a water spectral linewidth that was typically 10 Hz or less. The imaging parameters were as follows: a field of view = 24 mm × 24 mm, matrix size = 64 × 64, and slice thickness = 5 mm. Before the SL and CEST experiments, a T_1 map was obtained using an inversion-recovery sequence. In addition, the B_1 field was also mapped for calibration of the transmit power (25). With our volume coil, the B_1 map showed fairly good spatial homogeneity: the variation of B_1 was less than 10% across all pixels within the samples (data not shown).

For SL and CEST experiments, the CE contrast was first generated by the SL or CEST preparation (Fig. 1a); then, the residue magnetizations in the *X*–*Y* plane were dephased with crushing gradients; and finally, images were acquired with a spin-echo echo-planar imaging technique using an echo time of 42 msec. For on-resonance $R_{1\rho}$ dispersion experiments, SL was either achieved with the sequence shown in Fig. 1a for $\Omega = 0$ or with an adiabatic SL pulse sequence (25); the results were highly similar and are not distinguished here. $R_{1\rho}$ dispersion was measured for 10 $\omega_{1,\ SL}$ values of ~1110, 1570, 2220, 3140, 4440, 6280, 8880, 12,560, 17,760, and 25,120 rad/sec. At each $\omega_{1,\ SL}$, 14 TSL values, ranging between 0 and 330 msec, were acquired with a repetition time of 8 sec and a echo time of 42 msec. For CEST and SL *Z*-spectra measurements, images were collected within ±10 ppm of the water resonance, with the Rabi frequency of a 4-sec SL or CEST saturation pulse ($\omega_{1,\ SL}$ or $\omega_{1,\ CEST}$) = ~1100 rad/sec, and the repetition time was 18 sec. At each offset frequency, the SL flip angle θ was adjusted according to $\theta = \arctan(\omega_{1,SL} / \Omega)$. For the calculation of SLR and MTR, control M_0 images were acquired at the offset frequencies of ±300 ppm.

Three sets of MRI phantom experiments were performed.

Experiment I: On-Resonance $R_{1\rho}$ Dispersion and CEST Studies of Nicotinamide and Glucose with Different Concentrations

To evaluate whether SL and CEST contrast is sensitive to CEs in the slow- and intermediate-exchange regimes and to labile proton concentrations, 20, 50, 100, and 200 mM nicotinamide (Nic) and glucose (Glc) were dissolved in 1× phosphate-buffered saline (PBS) and titrated to pH of 7.4. As described in Introduction, the amide and hydroxyl protons are expected to be in the slow- and intermediate-exchange regimes, respectively. On-resonance $R_{1\rho}$ dispersions and CEST *Z*-spectra were obtained.

Experiment II: On-Resonance $R_{1\rho}$ Dispersion and CEST Studies of Glutamate with Various pH Values

To systematically study the exchange rate dependence of SL and CEST measurements, 50 mM glutamate (Glu) was dissolved in PBS and titrated to pH values of 3.1, 3.8, 4.5, 5.2, 5.9, 6.4, 6.9, 7.4, 7.9, 8.4, 9.1, and 9.8. The chemical shift between the amine (—NH_2) proton and water is 3.0 ppm (2). On-resonance $R_{1\rho}$ dispersions and CEST *Z*-spectra were obtained.

Experiment III: SL and CEST Z-Spectra of Nicotinamide and Glucose with Different pH Values

To compare the *Z*-spectra of SL and CEST, 100 mM Nic was dissolved in PBS and titrated to pH values of 7.4, 7.8, and 8.4, and 100 mM Glc was dissolved in PBS and titrated to pH values of 5.6 and 7.0. SL and CEST *Z*-spectra were obtained at ω_1 of ~1100 rad/sec, and on-resonance $R_{1\rho}$ dispersions were also measured with varying $\omega_{1,\ SL}$.

Data Analysis and Numerical Simulations

For each $\omega_{1,\ SL}$, on-resonance $R_{1\rho}$ maps were calculated by pixel-wise fitting of multi-TSL data to monoexponential signal decay with respect to TSL. One 5 × 5 mm^2 region of interest was selected for each sample, where all data were averaged. The CEST and off-resonance SL contrasts were estimated by calculating MTR_{asym} and SLR_{asym} using Eqs. 2 and 10, respectively. To obtain k_{ex}, p_B, and R_2, the on-resonance $R_{1\rho}$ dispersion data were fitted to Eq. 6, assuming a chemical shift of 1.2 ppm for glucose hydroxyl protons and 3.0 ppm for glutamate amine protons (2), respectively. Glucose hydroxyl protons have more than one CEST peak (9); for simplicity, we used only one chemical shift for data fitting in this work. Note that δ is expressed in rad/sec unit for the fitting of on-resonance $R_{1\rho}$ dispersion data to match with k_{ex} and ω_1 but is expressed in ppm units for CEST or SL *Z*-spectra, following the literature.

Experiment I

For glucose, the chemical exchanging parameters (k_{ex}, δ, p_B, and R_2), determined from on-resonance $R_{1\rho}$ dispersions, were used to simulate SLR_{asym} using Eqs. 8–10 for comparing with the experimental MTR_{asym}, and an effective $R_{ex,\ CEST}$ was constructed from the CEST *Z*-spectra using Eq. 12 with measured R_1 and fitted R_2. To simulate

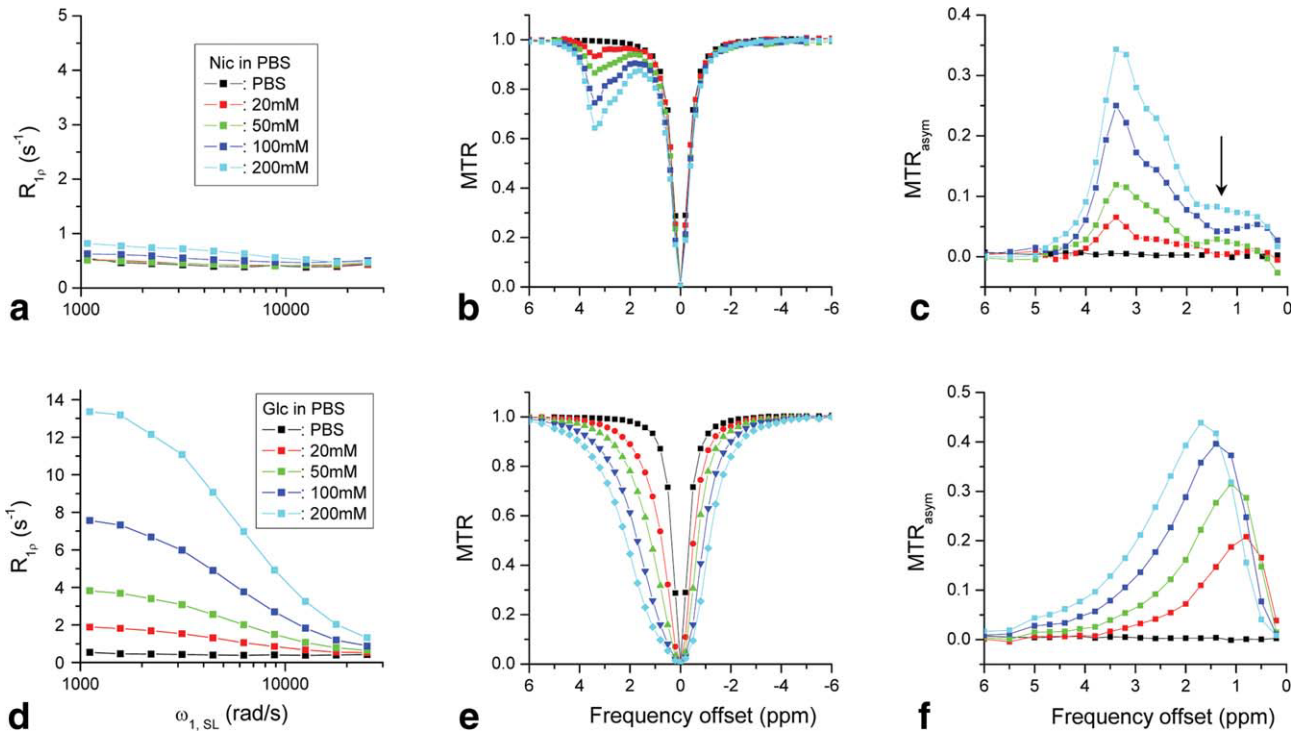

FIG. 2. On-resonance $R_{1\rho}$ dispersion, CEST *Z*-spectra, and the MTR_{asym} lineshapes for Nic (**a–c**) and Glc (**d–f**) samples with varied concentrations in PBS. The data of a pure PBS sample are also shown for comparison (black data points). For Nic with slow-exchanging amide protons, the $R_{1\rho}$ dispersion is small (a), but the CEST contrast is significant (b), and a well-defined MTR_{asym} peak appears at around 3.4 ppm for all concentrations (c). A plateau is observed in MTR_{asym} in the frequency offset range of 0.5–2 ppm (black arrow). For Glc with faster exchanging hydroxyl protons, the $R_{1\rho}$ dispersion is large and increases linearly with Glc concentration (d). The CEST *Z*-spectra (e) appear much broader compared with the Nic samples. The MTR_{asym} peak offset shifts, and the peak magnitude shows a nonlinear dependence with concentration (f). [Color figure can be viewed in the online issue, which is available at wileyonlinelibrary.com.]

SLR_{asym} of Nic, a δ of 3.4 ppm (8545 rad/sec) and k_{ex} of 100 sec^{-1} were assumed (8), and $R_{ex,\ CEST}$ was constructed using measured R_1 and assumed R_2 (see Results section). Then, the FWHM was obtained from fitting $R_{ex,\ CEST}$ to a Lorentzian lineshape, excluding data points close to the water resonance frequency (see Results below).

Experiment II

In all Glu pH phantoms, p_B should be constant, whereas k_{ex} is varied. Note that k_{ex} and p_B cannot be determined separately from on-resonance $R_{1\rho}$ dispersion data for samples when $k_{ex}/\delta \ll 1$. Thus, p_B of Glu was first fitted with a δ of 3.0 ppm (7540 rad/sec) from pH phantoms that gave the largest $R_{1\rho}$ dispersions (averaged from pH = 6.9, 7.4, and 7.9 samples, see Results below). Then, k_{ex} was determined with a fixed p_B for all pH phantoms. Similar to the data processing of Experiment I, SLR_{asym} was simulated and the linewidth of the $R_{ex,\ CEST}$ was calculated. To study the dependence on the chemical exchanging kinetics, on- and off-resonance $R_{1\rho}$ ($\Omega = 0$ and δ) were also simulated with $\delta = 3.0$ ppm, $p_B = 0.0014$, $R_1 = 0.35$ sec^{-1}, and $R_2 = 0.5$ sec^{-1} as a function of k_{ex}/δ for a few selected values of $\omega_{1,\ SL}$.

Experiment III

SL *Z*-spectra and SLR_{asym} were directly compared with the CEST *Z*-spectra and MTR_{asym}.

RESULTS

Experiment I: $R_{1\rho}$ and CEST Effects of Amide and Hydroxyl Protons

Figure 2 shows the on-resonance $R_{1\rho}$ dispersions, CEST *Z*-spectra, and MTR_{asym} for Nic (Fig. 2a–c) and Glc (Fig. 2d–f) phantoms with varying concentrations. As a control, the PBS solution was used (black squares), and no CE-related $R_{1\rho}$ dispersion or MTR_{asym} was observed. For Nic samples with slow-exchanging amide protons, the $R_{1\rho}$ dispersion is very small in the whole $\omega_{1,\ SL}$ range (Fig. 2a). In contrast, the CEST effect is apparent at the left side of the *Z*-spectra, where the MR signal dips at 3.4 ppm, more significantly with increasing Nic concentration (Fig. 2b). The spectra on the right side with negative frequency offset are independent of Nic concentration and overlap well with PBS, indicating minimal chemical exchanging effects. MTR_{asym} spectra had an increasing peak at 3.4 ppm with concentration (Fig. 2c) but was not symmetric around the peak. There is a plateau region in the 0.5–2 ppm range (arrow), which was also reported in a previous CEST study for amide protons (26).

Unlike Nic, Glc samples with a faster exchanging hydroxyl group show large $R_{1\rho}$ dispersions, where $R_{1\rho}$ decreases with the SL frequency $\omega_{1,\ SL}$ (Fig. 2d). $R_{1\rho}$ at each SL frequency increases almost linearly with Glc concentration. The signal drops in the CEST *Z*-spectra become very broad, and the exchange effect extends to

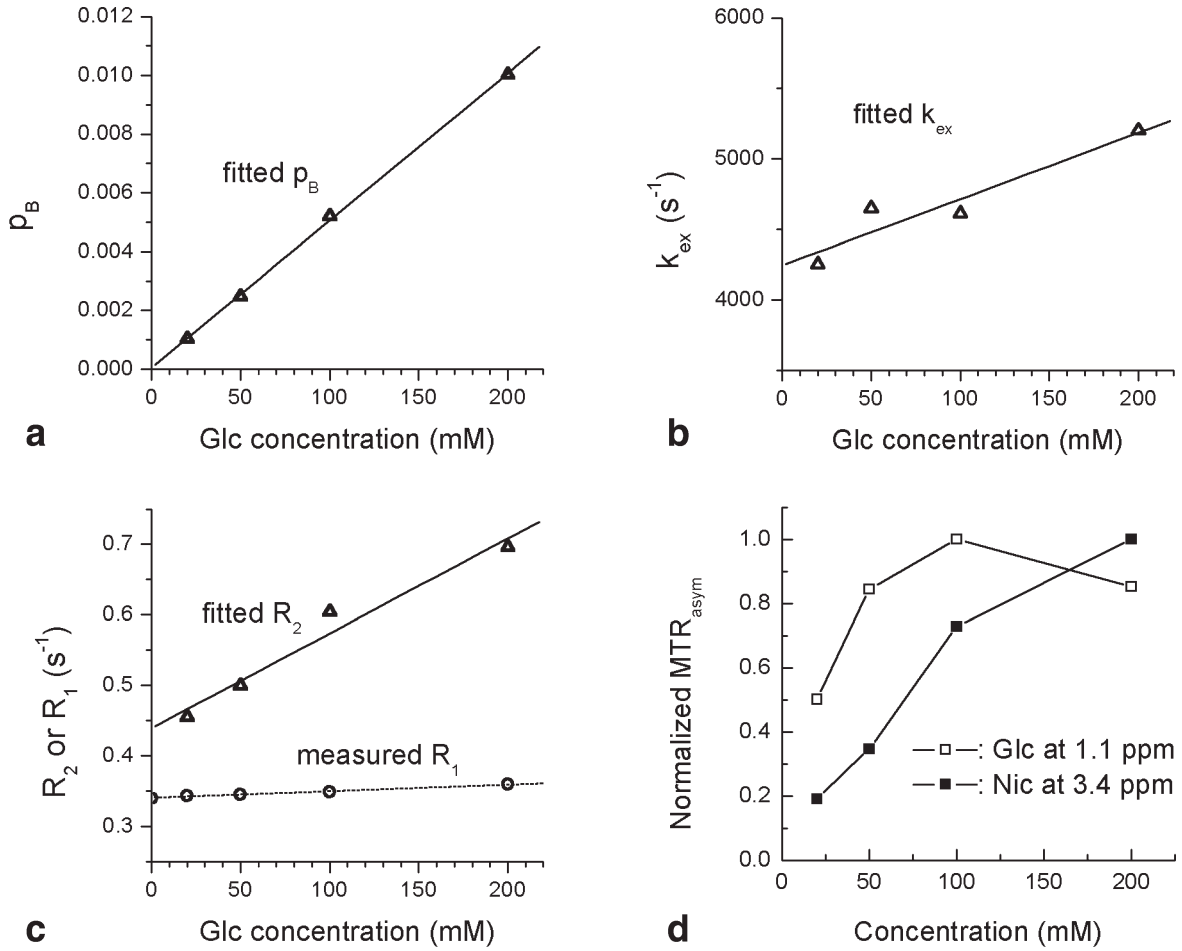

FIG. 3. **a–c**: Fitted results of the on-resonance $R_{1\rho}$ dispersion data as a function of Glc concentration, assuming $\delta = 1.2$ ppm (3016 rad/sec). The fitted p_B is proportional to the Glc concentraion (a). Fitted k_{ex} (b) and R_2 (c) increase with concentration, whereas the measured R_1 only increases weakly with concentration (c). **d**: For Nic and Glc, the MTR_{asym} peaks, obtained at 3.4 ppm for Nic and 1.1 ppm for Glc, were normalized. MTR_{asym} does not increase linearly with metabolite concentrations, especially for Glc.

negative frequency offsets, where the signals of Glc samples are much lower when compared with PBS (Fig. 2e). Because the exchanging effect presents on both sides of the water resonance, some CEST contrast would be sacrificed when two MTR signals of opposite frequency offset are subtracted for MTR_{asym}. The peak of MTR_{asym} spectra shifts toward a larger frequency offset with increasing Glc concentration (Fig. 2f).

In same metabolite phantoms with different concentrations, we expect a linear increase in p_B with concentration but a constant k_{ex}. Because large on-resonance $R_{1\rho}$ dispersions were only observed in the Glc samples, p_B, k_{ex}, and R_2 of glucose were obtained by fitting $R_{1\rho}$ dispersion data to Eq. 6 with a fixed δ of 1.2 ppm (3016 rad/sec) for glucose hydroxyl groups (see Fig. 3a–c). The fitted p_B is proportional to Glc concentration ($r^2 = 0.9994$) (Fig. 3a). The fitted k_{ex} and R_2 increase slightly with Glc concentration, probably because of the simplification of using a single chemical shift in our data fitting (Fig. 3b,c). It has been reported in a recent CEST study that the OH groups of Glc have three CE peaks with different frequency offsets (1–3 ppm from water) (9). Note that the measured R_1 is almost independent of the Glc concentration (Fig. 3c). For Glc samples in the intermediate-exchanging regime, the peak intensity of MTR_{asym} at 1.1 ppm does not monotonically increase with concentration (Fig. 3d). In contrast, for Nic samples in the slow-exchanging regime, the peak magnitude of MTR_{asym} at 3.4 ppm increases with concentration in a nearly linear manner.

Experiment II: SL and CEST at Varying CE Rate by Changing pH

The CE rate between amine ($-NH_2$) protons and water was systematically varied by changing pH values in 50-mM Glu samples. At lower pH, a slower exchange rate between two proton pools is expected. Significant on-resonance $R_{1\rho}$ dispersion was observed for samples with intermediate pH values ($5.9 \leq pH \leq 7.9$); the $R_{1\rho}$ dispersion peaked at a pH of ~7.4 but was small for both very high and low pH values (Fig. 4a,b). The half widths of $R_{1\rho}$ dispersion decreased with pH values (arrows in Fig. 4a,b). In the CEST experiments, the *Z*-spectra of Glu samples with pH = 9.1 and 9.8 were narrow and symmetric around the water frequency ($\Omega = 0$) (Fig. 4c),

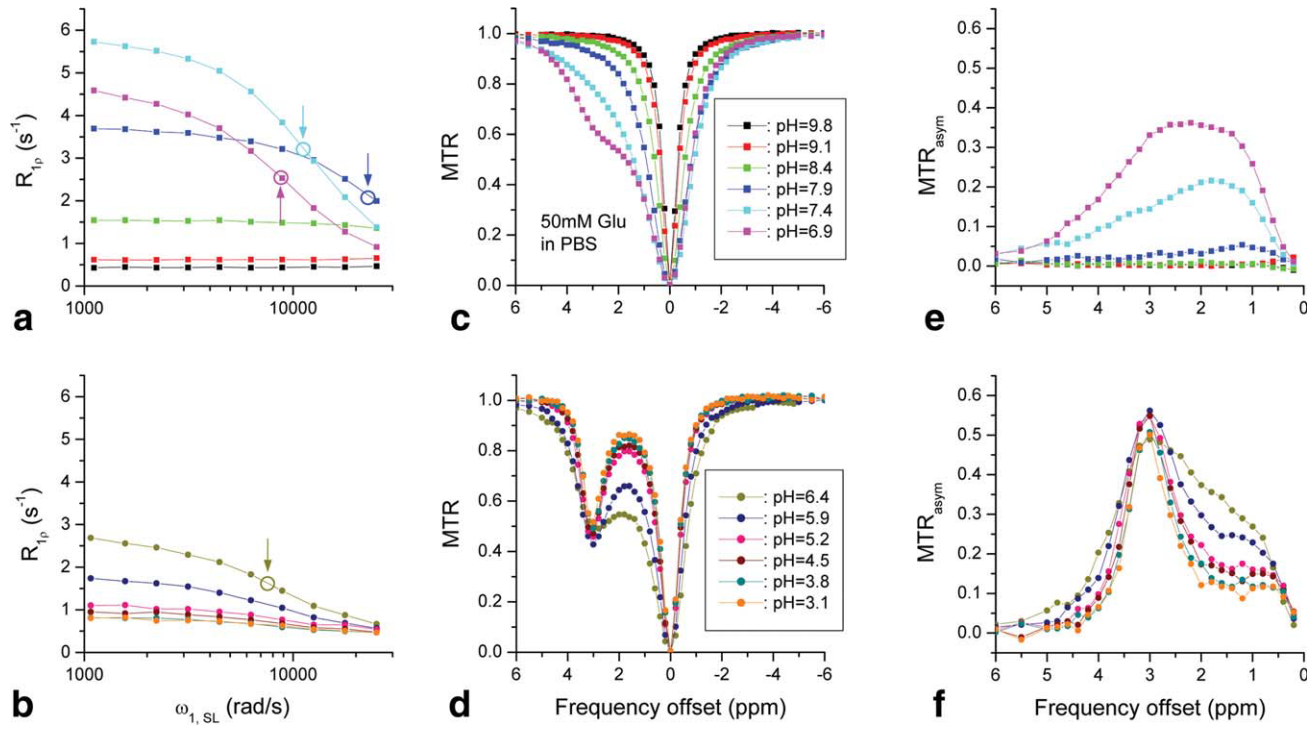

FIG. 4. On-resonance $R_{1\rho}$ dispersion (**a**, **b**), CEST *Z*-spectra (**c**, **d**), and MTR_{asym} lineshapes (**e**, **f**) for 50-mM Glu samples with varied pH. $R_{1\rho}$ dispersion is large for intermediate pH values but small for very high or low pH. The half width of the $R_{1\rho}$ dispersion decreases with pH (circles and arrows). The CEST *Z*-spectra are narrow and symmetric for high pH values (9.1 and 9.8); become broad and increasingly asymmetric for intermediate pH values; and show a sharp dip at 3.0 ppm for low pH values. For pH $\leq$ 5.9, the MTR_{asym} peaks at 3.0 ppm and the peak magnitude only reduces slightly with pH. For higher pHs, MTR_{asym} lineshape becomes broad and the peak shifts to a smaller frequency offset and decreases in magnitude.

similar to the PBS data in Fig. 2e. When pH decreased, *Z*-spectra became broader initially, increased the asymmetry around the water frequency (pH = 8.4–7.4, Fig. 4c), and then had an increased dip at 3.0 ppm (Fig. 4d). MTR_{asym} spectra were broad at pH = 7.4 and 6.9, and its peak shifted to 3.0 ppm for pH $\leq$ 6.4. The shapes of the MTR_{asym} spectra were similar for pH $\leq$ 5.2 but not symmetric around the 3-ppm peak (Fig. 4e,f).

Figure 5a shows the k_{ex} of Glu with pH $\leq$ 8.4, determined by fitting on-resonance $R_{1\rho}$ dispersions with a p_B of 0.00135 $\pm$ 0.0001 (n = 3), obtained from pH = 6.9, 7.4, and 7.9 data. As expected in a base-catalyzed exchange process, k_{ex} decreases with pH, similar to recent CEST measurements of amide protons (26). Given a δ of 3 ppm (7540 rad/sec), pH = 6.4–7.9 samples can be roughly ascribed to the intermediate-exchange regime, whereas samples with pH $\leq$ 5.9 and pH $\geq$ 8.4 are in the slow- and fast-exchange regimes, respectively. These results indicate that on-resonance $R_{1\rho}$ dispersion is most sensitive to the intermediate-exchange regime but much less to fast and slow exchanges (see Fig. 4a,b). In contrast, CEST with a relatively low $\omega_{1,\ CEST}$ is sensitive to slow to intermediate exchanges but more to slow exchanges (see Fig. 4c,d).

The k_{ex} values obtained from on-resonance SL were plotted against the MTR_{asym} of 3 ppm (Fig. 5b). MTR_{asym} is maximal at a k_{ex}/δ of ~0.1 (in the slow-exchange regime) and at a k_{ex} of ~1100 sec^{-1} (pH = 5.9), which matches well with the Rabi frequency of the applied saturation pulse $\omega_{1,\ CEST}$ (~1100 rad/sec). To compare the characteristics of on- and off-resonance SL, $R_{1\rho}$ on the resonance of water (Ω = 0) and labile proton (Ω = δ) were simulated as a function of k_{ex}/δ at a few selected $\omega_{1,\ SL}$ (Fig. 5c,d), with assumptions of R_1 = 0.35 sec^{-1}, R_2 = 0.5 sec^{-1}, δ = 3.0 ppm, and p_B = 0.0014. Although different parameters can change $R_{1\rho}$ values, the features of $R_{1\rho}$ vs. k_{ex}/δ curves remain. Note that $R_{1\rho}$ and $\omega_{1,\ SL}$ were scaled by $p_B\delta$ and δ, respectively. For on-resonance SL (Fig. 5c), the $R_{1\rho}$ peak starts from the intermediate-exchange regime for very small $\omega_{1,\ SL}$ and shifts to faster exchanges with increasing $\omega_{1,\ SL}$. Thus, on-resonance SL is less sensitive to slow CEs when compared with intermediate exchanges. For off-resonance SL with Ω = δ (Fig. 5d), $R_{1\rho}$ can be made to be sensitive to different k_{ex} values by variation of $\omega_{1,\ SL}$, and the peaks appear at k_{ex} = $\omega_{1,\ SL}$. The maximum $R_{1\rho}$ is reached at an intermediate-exchange domain with an intermediate SL frequency ($\omega_{1,\ SL}$ = k_{ex} = δ). This simulation can be understood as a tuning of $R_{1\rho}$ to certain k_{ex} values when there is a wide distribution of k_{ex} values. In contrast to on-resonance SL, off-resonance $R_{1\rho}$ with a small $\omega_{1,\ SL}$ can be tuned to slow exchanges, where a faster CE contribution is suppressed. For example, for our Glu data with $\omega_{1,\ SL}$ = 1100 rad/sec (which were obtained from Glu with a pH of 5.9), δ = 3 ppm (7540 rad/sec), and $\omega_{1,\ SL}/\delta$ = 0.14, the peak of the $R_{1\rho}$ curve (red) appears at k_{ex}/δ ~ 0.14 in the slow-exchange regime.

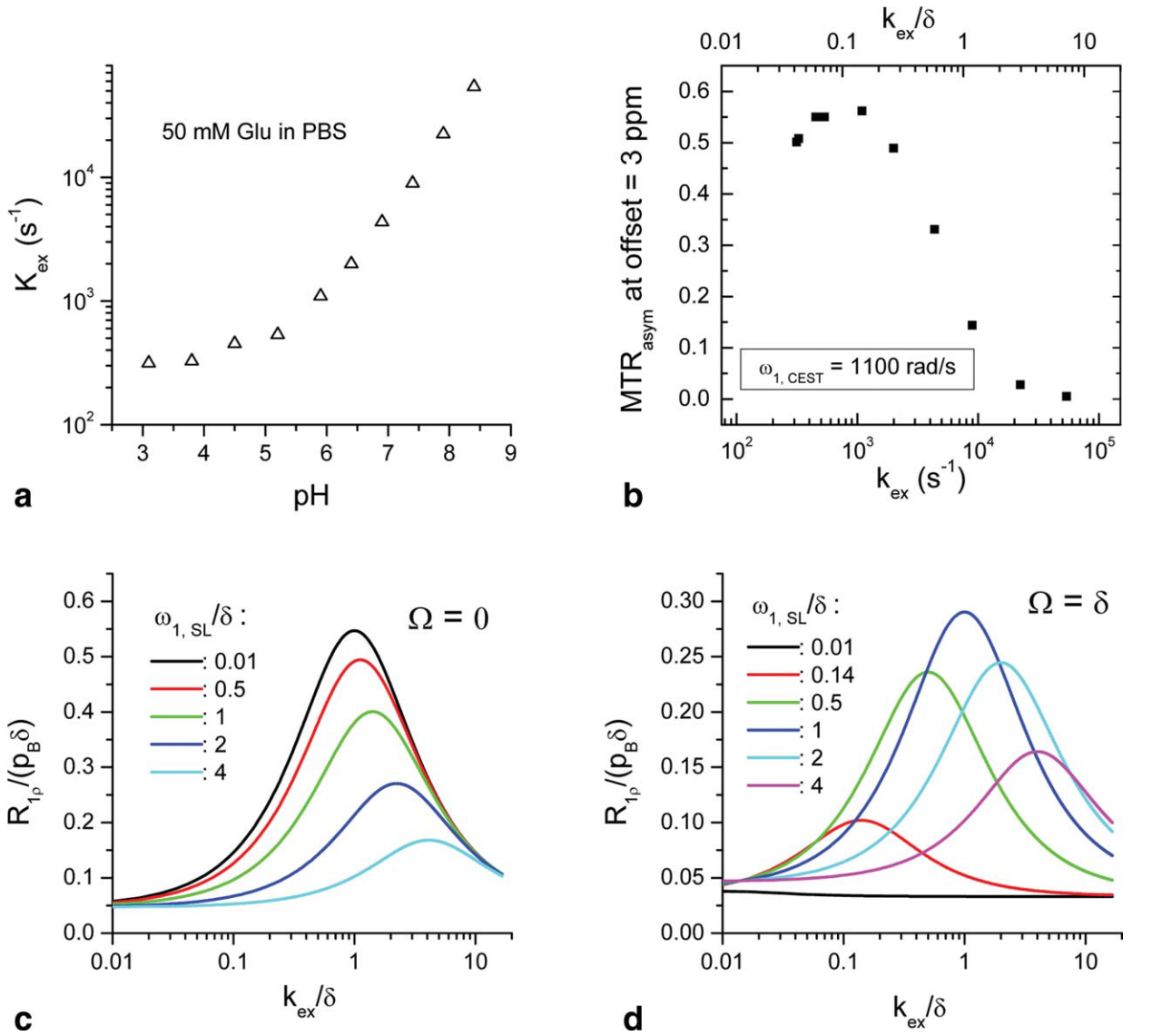

FIG. 5. **a**: Fitted k_{ex} as a function of pH for 50-mM Glu samples, assuming $\delta = 7540$ rad/sec (3 ppm). **b**: For Glu samples with varying pHs, the MTR_{asym} at a frequency offset of 3 ppm is plotted as a function of the fitted k_{ex}, which shows a peak around $k_{ex}/\delta \sim 0.1$ at the slow-exchange regime. The peak k_{ex} is ~1100 sec^{-1} and matches with the frequency of the applied saturation power (1100 rad/sec). **c**, **d**: Simulation of on and off resonance ($R_{1\rho}/p_B\delta$) as a function of k_{ex}/δ for selected $\omega_{1, SL}/\delta$ values, assuming $\delta = 3$ ppm, $p_B = 0.0014$, $R_1 = 0.35$ sec^{-1}, and $R_2 = 0.5$ sec^{-1}. On-resonance $R_{1\rho}$ can only be tuned to the intermediate chemical exchange process with a small $\omega_{1, SL}$ and a faster exchange with a higher $\omega_{1, SL}$ (c). In contrast, off-resonance ($\Omega = \delta$) $R_{1\rho}$ can be tuned to slow, intermediate, and fast exchanges with small, intermediate, and large $\omega_{1, SL}$ values, respectively (d). [Color figure can be viewed in the online issue, which is available at wileyonlinelibrary.com.]

Experiment III: Similarity of SL and CEST *Z*-Spectra

The SL *Z*-spectra (solid lines in Fig. 6a,d) of the Nic, Glc, and PBS samples were compared with the corresponding CEST *Z*-spectra (dashed lines). These two spectra match very well except at small frequency offsets (see Insets). SLR at a given offset is always higher than MTR. For example, for Nic at pH = 7.4 (Fig. 6a) and PBS (Fig. 6d), 7 and 13% of the MR signal remained after a 4-sec on-resonance SL pulse ($\Omega = 0$), respectively, whereas the CEST signals were zero because of the direct water saturation effect. The MTR_{asym} and the SLR_{asym} spectra (Fig. 6b,e) also show high similarity. The difference between MTR_{asym} and SLR_{asym} spectra close to 0 ppm was small, indicating that the subtraction of MTR between opposite offset frequencies is an effective approach to cancel the majority of the spillover effect in CEST *Z*-spectra. In the SLR_{asym} and MTR_{asym} of Nic samples, there is a shift of the peak from 3.4 to 2.6 ppm (arrows) with increasing pH from 7.8 to 8.4. In both the SLR_{asym} and MTR_{asym} spectra of the Glc samples, more than one —OH peak can be discerned (for pH = 5.6, arrows), similar to a previous report (9). To compare with off-resonance SL and CEST data, on-resonance $R_{1\rho}$ dispersions were plotted in Fig. 6c,f. The $R_{1\rho}$ dispersion in Nic and Glc increases significantly with pH because of an increase of k_{ex} from slow- to intermediate-exchange regimes.

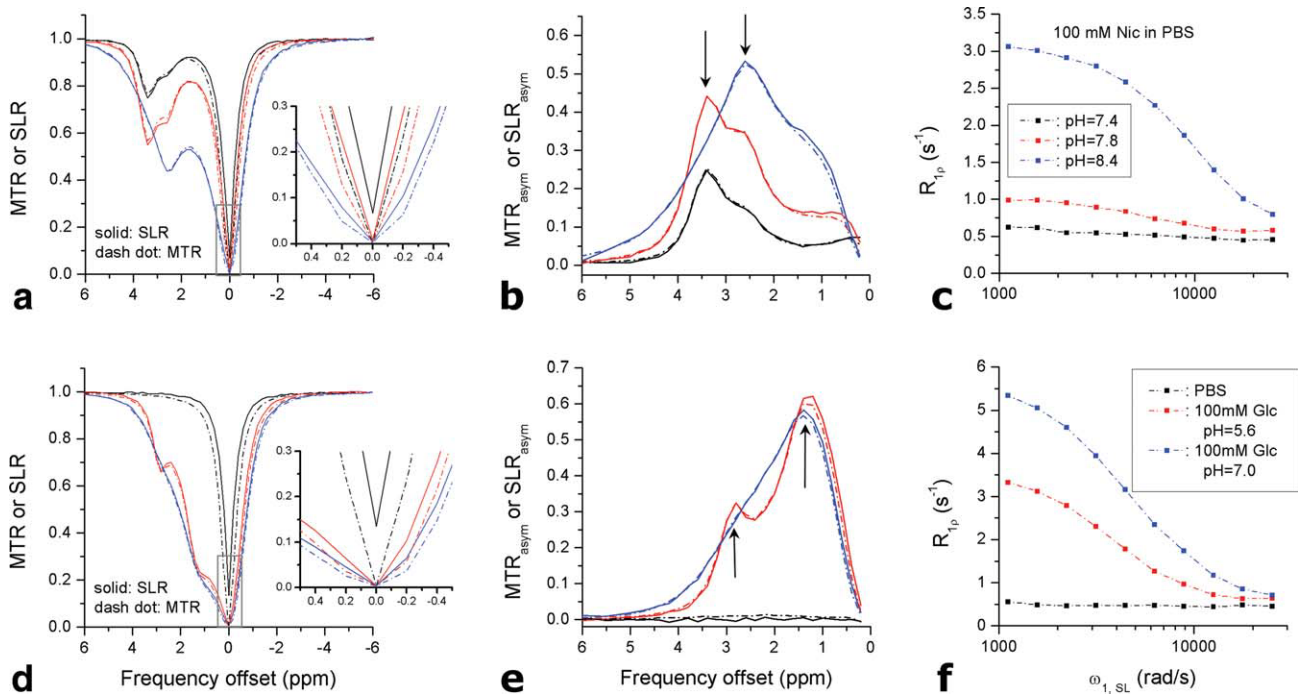

FIG. 6. SL *Z*-spectra (solid) and CEST *Z*-spectra (dashed), the SLR_{asym} (solid) and MTR_{asym} (dashed) lineshapes, and on-resonance $R_{1\rho}$ dispersions for Nic (**a**–**c**) and Glc (**d**–**f**) samples with varied pH in PBS. SL and CEST spectra match well for large frequency offsets, and a small difference is observed when close to the water resonance (a and d). Insets: the enlarged SL and CEST Z-spectra show that the CEST signals are smaller than those of SL because of direct water saturation. SLR_{asym} and MTR_{asym} also match well for all samples (b and e), and more than one peak is detected for both Nic and Glc (arrows). On-resonance $R_{1\rho}$ dispersions of both Nic and Glc are very sensitive to pH (c and f). [Color figure can be viewed in the online issue, which is available at wileyonlinelibrary.com.]

Simulated SLR_{asym} Spectra vs. Experimental MTR_{asym} Spectra

The similarity in the SL and CEST *Z*-spectra suggests that the experimental CEST data may be explained by Trott and Palmer's SL model. SLR_{asym} values (lines) were simulated with the parameters obtained from on-resonance $R_{1\rho}$ dispersions for Glu and Glc (Fig. 7a,b) or assumed values for Nic (Fig. 7c) and compared with experimental CEST MTR_{asym} data (data points). The Nic on-resonance $R_{1\rho}$ dispersion data cannot be fitted robustly because of its low sensitivity (see Fig. 2a). Overall, the match between simulated SLR_{asym} and experimental MTR_{asym} is very good, indicating that the CEST *Z*-spectra can be explained by the SL model.

Effective R_{ex} Obtained from CEST *Z*-Spectra

On-resonance $R_{1\rho}$ dispersion provides one way of characterizing the CE process that is well suited for the intermediate-exchange regime. However, it is difficult to apply to a slow-exchange regime because of reduced sensitivity, and it is also difficult to distinguish from multiple-exchanging sites with different chemical shifts. Alternatively, R_{ex} can be obtained from SL *Z*-spectra (Eq. 11) or CEST *Z*-spectra (Eq. 12). Unlike CEST *Z*-spectra (see Fig. 4c,d), the $R_{ex,\ CEST}$ of Glu samples with varied pH showed a peak at 3 ppm (Fig. 8a). The data close to water resonance were not reliable because of the direct water saturation effect and thus were excluded. The broadening of the $R_{ex,\ CEST}$ curve is sensitive to exchange rates; the FWHM of the Lorentzian shape is highly correlated with $\sqrt{\omega_{1,CEST}^2 + k_{ex}^2}$ (Fig. 8b), where k_{ex} is the fitted exchange rate from on-resonance $R_{1\rho}$ dispersion data (Fig. 5a) and the applied $\omega_{1,\ CEST} = 1100$ rad/sec. This indicates that k_{ex} can be obtained from CEST *Z*-spectra (more accurately $R_{ex,\ CEST}$).

When the linewidth of $R_{ex,\ CEST}$ is constant (i.e., k_{ex} constant), the peak amplitude of R_{ex} is proportional to the labile proton population. Figure 8c,d shows the $R_{ex,\ CEST}$ converted from Nic and Glc CEST *Z*-spectra data with four concentrations (see Fig. 2b,e). Although R_2 has not been calculated for Nic samples, on-resonance R_{ex} is minimal when $\omega_{1,\ SL} \gg \delta$ and $p_B k_{ex} < 1\ sec^{-1}$ (see Eq. 5 and Fig. 7c). Therefore, R_2 can be approximated well with the measured $R_{1\rho}$ at a large $\omega_{1,\ SL}$. The averaged $R_{1\rho}$ is $0.48 \pm 0.02\ sec^{-1}$ ($n = 4$) at $\omega_{1,\ SL} = 25{,}120$ rad/sec (Fig. 2a), so we used $R_2 = 0.5\ sec^{-1}$ for simplicity. The $R_{ex,\ CEST}$ values of Nic and Glc show a peak at 3.4 and 1.1 ppm, respectively. The peak magnitude of $R_{ex,\ CEST}$ increases with concentration almost linearly for both Nic and Glc (Fig. 8e). The averaged FWHM of $R_{ex,\ CEST}$ for the four Glc is $4272 \pm 628\ sec^{-1}$, and consequently, k_{ex} is estimated to be $4147\ sec^{-1}$ for a $\omega_{1,\ CEST}$ of 1100 rad/sec, slightly smaller than $k_{ex} = 4680 \pm 390\ sec^{-1}$ ($n = 4$, from Fig. 3b) obtained from the on-resonance $R_{1\rho}$ dispersion data. Nic samples give an averaged $R_{ex,\ CEST}$ FWHM of $1156 \pm 125\ sec^{-1}$, which is not much larger than the applied $\omega_{1,\ CEST}$, indicating that k_{ex} is very small. To accurately determine slow k_{ex}, it is necessary to use a small $\omega_{1,\ CEST}$, similar to or less than k_{ex}.

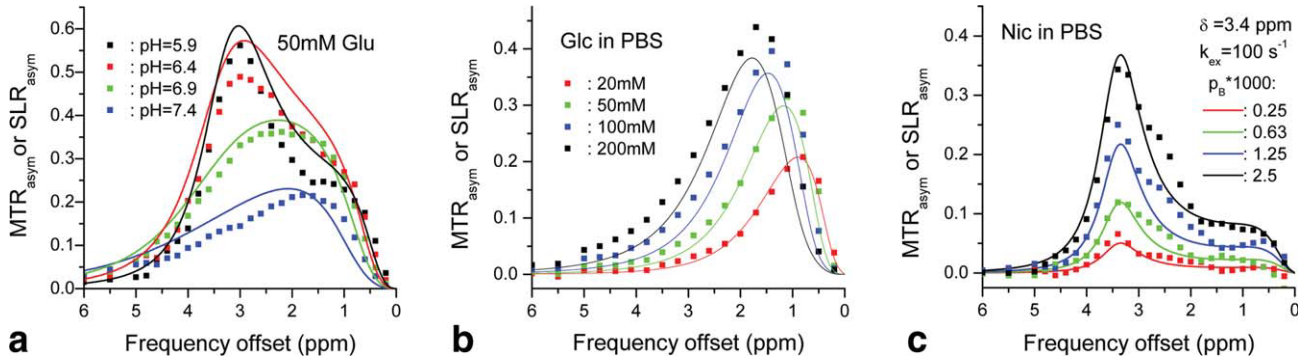

FIG. 7. Simulated SLR_{asym} spectra lines are compared with the experimental MTR_{asym} (squares) for 50-mM Glu samples with varied pH (**a**) and for Glc (**b**) and Nic (**c**) samples with varied concentrations. In (a) and (b), the parameters used for the simulation of SLR_{asym} were obtained by the fitting of on-resonance $R_{1\rho}$ dispersion. In (c), k_{ex} of 100 sec^{-1} and δ_B of 3.4 ppm (8545 rad/sec) were assumed for Nic samples. [Color figure can be viewed in the online issue, which is available at wileyonlinelibrary.com.]

DISCUSSION

Both on- and off-resonance SL approaches can be applied to studies of CE. Although on- and off-resonance SL is sensitive to intermediate exchanges, off-resonance SL can also be tuned to slow exchanges by adjusting $\omega_{1,SL}$ (Fig. 5c,d). At high magnetic fields, such as 9.4 T, the on-resonance SL is more sensitive to hydroxyl and amine proton exchanges than amide protons, whereas off-resonance SL experiments with a low irradiation power are more sensitive to amide protons. Hence, the parameters of the SL technique, such as the SL pulse power and SL frequency offset, can be adjusted to provide optimal contrast and probe information of the tissue microenvironment for specific applications. When multiple exchangeable protons exist, such as in vivo, it would be difficult to determine the source of a CE contrast in on-resonance SL. Off-resonance SL experiments may be selective to certain types of exchanging protons within the slow-exchange domain, such as the amide protons, by locking the water magnetization on that specific Larmor

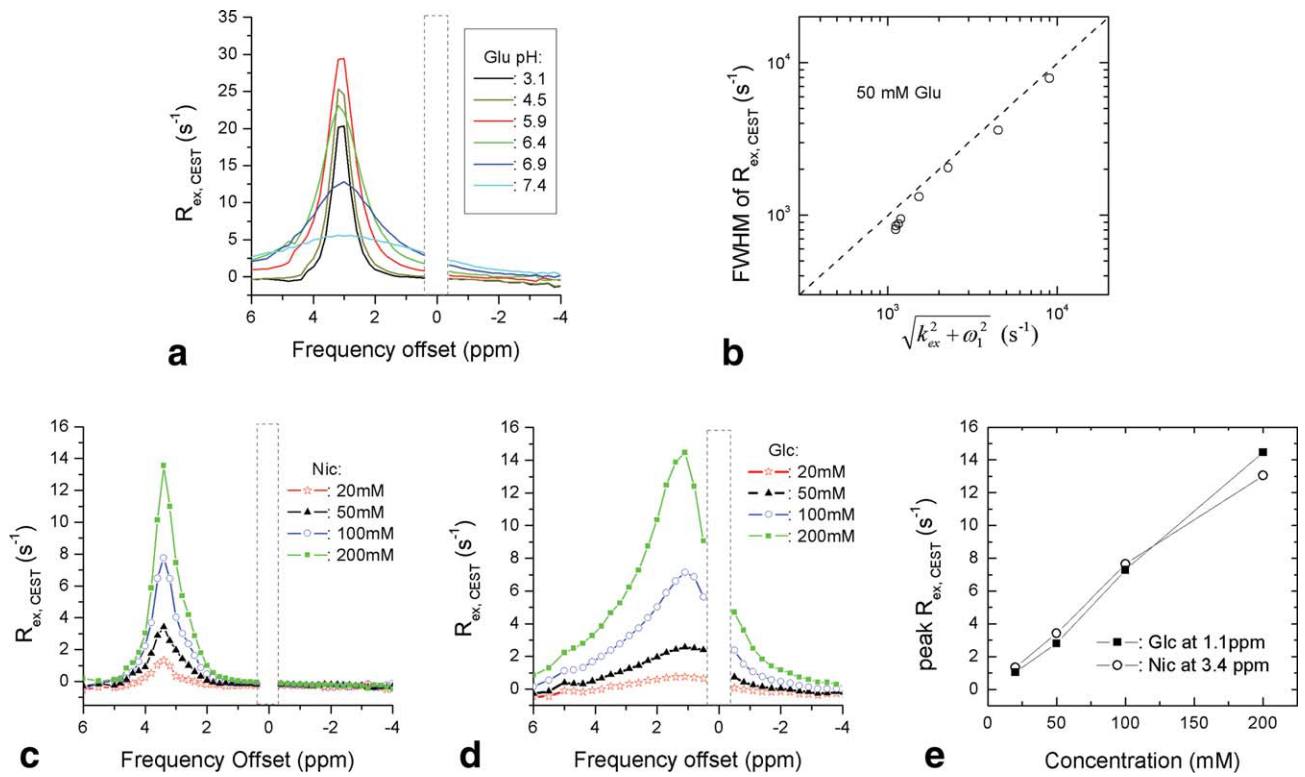

FIG. 8. **a**: Effective $R_{ex, CEST}$, defined in Eq. 12, was calculated from the CEST *Z*-spectra of 50-mM Glu samples with pH between 3.1 and 7.4. The linewidth of $R_{ex, CEST}$ decreases with pH, and the peak of $R_{ex, CEST}$ is reached for the pH = 5.9 sample. The data at frequency offsets close to zero were excluded because of the direct water saturation effect. **b**: The linewidths of $R_{ex, CEST}$ in (a) were fairly close to those fit from the on-resonance $R_{1\rho}$ dispersion data. Effective $R_{ex, CEST}$ was also calculated for Nic (**c**) and Glc (**d**) samples with four concentrations. The peak of $R_{ex, CEST}$ increases linearly with metabolite concentration (**e**). [Color figure can be viewed in the online issue, which is available at wileyonlinelibrary.com.]

frequency. However, the interpretation of the observed CE contrast should remain cautious, because other intermediate- or fast-exchanging protons (even if with a different Larmor frequency) can still contribute because of their broad R_{ex} spectrum.

Because off-resonance SL is similar to CEST, CEST spectra can be used to measure slow- to intermediate-exchange processes and can be explained approximately with the SL theoretical model. This is plausible, because both techniques measure the same CE phenomena, with slightly different experimental approaches (Fig. 1a). During the long off-resonance radiofrequency pulse common to both approaches, the water magnetization experiences an effective B_1, tilted at an angle $\theta = \arctan(\omega_1 / \Omega)$ from the B_0 direction. With the SL technique, water magnetization is first flipped to and then locked to the $B_{1,\,eff}$ direction. In a CEST experiment, without the initial flip, the magnetization along the $B_{1,\,eff}$ direction relaxes with a time constant $T_{1\rho}$, and the component perpendicular to the $B_{1,\,eff}$ oscillates and decays with a time constant $T_{2\rho}$ (27). Thus, a CEST experiment can be considered an off-resonance SL with imperfect SL: the water spins are pseudo-locked to $B_{1,\,eff}$, precessing on the surface of a cone with a half angle of θ (Fig. 1d). Such a pseudo-SL can be a good approximation as long as θ is very small; i.e., $\omega_{1,\,CEST} \ll \Omega$. Thus, to study the CE effects, the SL technique is more versatile and can be applied to a frequency offset close to water and also for on-resonance cases.

SL and CEST results of simple metabolite phantoms can be explained well using Trott and Palmer's AP model. Previous SL models mostly assumed a fast-exchange limit and, hence, could not be applied to slower exchanging protons. The exchange-related relaxation rate under fast exchange approximation is (24):

$$R_{ex}(\Omega, \omega_{1,SL}) = \frac{p_B \cdot \delta^2 \cdot k_{ex}}{\Omega^2 + \omega_{1,SL}^2 + k_{ex}^2}, \quad [13]$$

Thus, p_B and δ cannot be determined separately, so the application is further limited. One simplification taken in Trott and Palmer's model is to use population-averaged values of R_1 and R_2 for protons of the two exchanging sites and ignore their differences, which may affect the accuracy in the estimation of k_{ex} and p_B if such differences are significant. Nevertheless, this SL model is quite useful and can be applied to slow-, intermediate-, and fast-exchanging regimes, enabling quantification of CE parameters. The AP model is also compatible with current CEST models. For example, if the SL pulse is applied on the labile proton ($\Omega = \delta$), under the conditions $k_{ex} \ll \omega_{1,\,SL}$ and $R_2 \ll R_{ex}$, the steady-state solution equation [9] can be simplified to:

$$\frac{M(\Omega = \delta)}{M_0} = \frac{1}{1 + p_B \cdot k_{ex} \cdot T_1} \quad [14]$$

which is equivalent to the steady-state solution obtained from the CEST experiment [Eq. 23 in (28)]. From Eq. 9, one can also find that

$$\frac{M_0}{M_{offset}} - 1 = \frac{R_2 + R_{ex}}{R_1} \cdot \frac{\omega_1^2}{\Omega^2}, \quad [15]$$

If the SL pulse is applied on the labile proton and under the assumption $R_2 \ll R_{ex}$, the equation above can be converted to

$$\frac{M_{offset}}{M_0 - M_{offset}} = \frac{R_1 k_{ex}}{p_B} \cdot \left(\frac{1}{k_{ex}^2} + \frac{1}{\omega_1^2}\right), \quad [16]$$

which is identical to the omega-plot equation derived by Dixon et al. (29).

To quantify the concentration of labile nonwater protons or the pH of a tissue microenvironment in conventional CEST approaches, McMahon et al. (26) and Sun (30) performed CEST experiments with several different $\omega_{1,\,CEST}$ values and fit the experimental results to the CEST model with a number of assumed parameters. McMahon et al. (26) also proposed to measure the MTR as a function of saturation time and fit to theoretical models. Dixon et al. proposed another method to measure the exchange rate and labile proton population. From Eq. 16, a plot of $M_{offset}/(M_0 - M_{offset})$ at a labile proton frequency vs. $1/\omega_1^2$ gives the k_{ex} for the X-intercept and the ratio of k_{ex} and p_B for the slope. The frequency offset of the targeted labile proton should be known in all these methods.

Our results show that the effective relaxation rate $R_{ex,\,CEST}(\Omega)$, converted from the CEST Z-spectra data, is well suited for the characterization of CEs in slow and intermediate regimes. Because a complete Z-spectrum is used for data fitting, a priori knowledge of frequency offset of the labile proton is unnecessary. $R_{ex,\,CEST}$ is proportional to the labile proton population in both slow- and intermediate-exchange regimes, and $R_{ex,\,CEST}$ peak intensity increases with labile proton concentration. The linewidth of $R_{ex,\,CEST}$ is closely related to exchange rates and, consequently, pH. Note that for in vivo applications, confounding effects such as magnetization transfer effects from large solid-like macromolecules also affect the Z-spectra; hence, the extraction and analysis of R_{ex} become much more complicated.

The asymmetrical MTR analysis from the CEST Z-spectra provides a convenient measure of CE contrast and has been proven to be successful in the slow-exchange regime, but it should be noted that MTR_{asym} is not a monotonic function of k_{ex} or pH; for example, it can increase or decrease with k_{ex} depending on the choice of saturation pulse power. Under our condition, MTR_{asym} peaks at $k_{ex} = \omega_{1,\,CEST}$; therefore, with decreasing k_{ex}, MTR_{asym} will decrease for $k_{ex} < \omega_{1,\,CEST}$ but increase for $k_{ex} > \omega_{1,\,CEST}$. Thus, the saturation pulse power should be carefully chosen if MTR_{asym} is used as a biomarker to detect in vivo pH changes. A similar issue has also been pointed out in a previous CEST study with numerical simulations (26). In the intermediate-exchange regime, the interpretation of MTR_{asym} is highly complicated. (i) The peak offset of MTR_{asym} shifts with varying labile proton concentrations and pHs, making it hard to interpret the data. (ii) Because MTR_{asym} is essentially a measure of imaging contrast, it cannot be higher than 100% (9). With increasing concentrations of labile protons, MTR_{asym} does not increase linearly in the slow-exchange regime, but this problem becomes more severe in the intermediate-exchange regime, where it can even

decrease at small frequency offsets. (iii) If the CEST *Z*-spectrum is broad and the CE contrast extends to negative offset frequencies beyond the water resonance frequency (see Fig. 2e), the subtraction method for the MTR_{asym} may lead to a significant loss of sensitivity, especially at smaller frequency offsets (see Fig. 2e vs. 2f).

One difficulty of in vivo applications of endogenous CE contrast is its limited sensitivity. The reported MTR_{asym} of amide proton transfer at 3.5 ppm is about 2% for 1.5 T and 4% for 3 T (5,31). To enhance the CE sensitivity, a larger exchange rate, a larger difference in the Lamor frequencies of exchanging protons, and a higher magnetic field are favorable. Based on our results, 1 mM glucose and glutamate can contribute up to an on-resonance $R_{1\rho}$ of 0.07 and $\sim$0.1 sec^{-1}, repesctively. With an SL B_1 of a few hundred hertz and a continuous wave SL pulse length of 50 msec [close to the the $T_{1\rho}$ of brain cortical tissue at 9.4 T (25,32)], this relaxation rate would translate to a signal change of 0.35–0.5%, which could be well detectable by many in vivo experiments.

CONCLUSIONS

To compare the characteristics of on- and off-resonance SL and CEST experiments, metabolite phantoms were studied in the slow-, intermediate-, and fast-exchanging regimes and with varied concentrations. The off-resonance SL approach exhibits similar results as the CEST experiment when the direct water saturation effect is small. On-resonance SL is sensitive to intermediate proton exchanges, whereas off-resonance SL and CEST experiments can be tuned to slow-exchanging protons using a low-power SL or saturation pulse. SL and CEST data can be explained well using Trott and Palmer's model with AP approximation. From the CEST *Z*-spectra, an effective exchange relaxation rate, R_{ex}, can be constructed and can be used to quantitatively characterize the chemical exchanging process. The conventional parameter MTR_{asym} provides an easy measure of CE contrast, but unlike R_{ex}, it is not a monotonic function of exchange rate (and pH); its application in the intermediate-exchange regime becomes problematic.

ACKNOWLEDGMENT

The authors thank Kristy Hendrich for maintaining the 9.4-T system.

REFERENCES

1. Ward KM, Aletras AH, Balaban RS. A new class of contrast agents for MRI based on proton chemical exchange dependent saturation transfer (CEST). J Magn Reson 2000;143:79–87.
2. Zhou JY, van Zijl PCM. Chemical exchange saturation transfer imaging and spectroscopy. Prog Nucl Magn Reson Spectrosc 2006;48: 109–136.
3. Davis DG, Perlman ME, London RE. Direct measurements of the dissociation-rate constant for inhibitor-enzyme complexes via the T-1-Rho and T-2 (CPMG) methods. J Magn Reson B 1994;104:266–275.
4. Fischer MWF, Majumdar A, Zuiderweg ERP. Protein NMR relaxation: theory, applications and outlook. Prog Nucl Magn Reson Spectrosc 1998;33:207–272.
5. Zhou JY, Payen JF, Wilson DA, Traystman RJ, van Zijl PCM. Using the amide proton signals of intracellular proteins and peptides to detect pH effects in MRI. Nat Med 2003;9:1085–1090.
6. Sun PZ, Zhou JY, Sun WY, Huang J, van Zijl PCM. Detection of the ischemic penumbra using pH-weighted MRI. J Cereb Blood Flow Metab 2007;27:1129–1136.
7. Jokivarsi KT, Grohn HI, Grohn OH, Kauppinen RA. Proton transfer ratio, lactate, and intracellular pH in acute cerebral ischemia. Magn Reson Med 2007;57:647–653.
8. Liepinsh E, Otting G. Proton exchange rates from amino acid side chains—implications for image contrast. Magn Reson Med 1996;35: 30–42.
9. van Zijl PCM, Jones CK, Ren J, Malloy CR, Sherry AD. MRI detection of glycogen in vivo by using chemical exchange saturation transfer imaging (glycoCEST). Proc Natl Acad Sci USA 2007;104:4359–4364.
10. Ling W, Regatte RR, Navon G, Jerschow A. Assessment of glycosaminoglycan concentration in vivo by chemical exchange-dependent saturation transfer (gagCEST). Proc Natl Acad Sci USA 2008;105: 2266–2270.
11. Duvvuri U, Goldberg AD, Kranz JK, Hoang L, Reddy R, Wehrli FW, Wand AJ, Englander SW, Leigh JS. Water magnetic relaxation dispersion in biological systems: the contribution of proton exchange and implications for the noninvasive detection of cartilage degradation. Proc Natl Acad Sci USA 2001;98:12479–12484.
12. Regatte RR, Akella SVS, Borthakur A, Kneeland JB, Reddy R. Proteoglycan depletion-induced changes in transverse relaxation maps of cartilage: comparison of T2 and T1 rho. Acad Radiol 2002;9: 1388–1394.
13. Akella SVS, Regatte RR, Borthakur A, Kneeland JB, Leigh JS, Reddy R. T1 rho MR Imaging of the human wrist in vivo. Acad Radiol 2003; 10:614–619.
14. Santyr GE, Henkelman RM, Bronskill MJ. Spin locking for magnetic resonance imaging with application to human breast. Magn Reson Med 1989;12:25–37.
15. Markkola AT, Aronen HJ, Paavonen T, Hopsu E, Sipila LM, Tanttu JI, Sepponen RE. Spin lock and magnetization transfer imaging of head and neck tumors. Radiology 1996;200:369–375.
16. Markkola AT, Aronen HJ, Paavonen T, Hopsu E, Sipila LM, Tanttu JI, Sepponen RE. T1 rho dispersion imaging of head and neck tumors: a comparison to spin lock and magnetization transfer techniques. J Magn Reson Imaging 1997;7:873–879.
17. Poptani H, Duvvuri U, Miller CG, Mancuso A, Charagundla S, Fraser NW, Glickson JD, Leigh JS, Reddy R. T1(rho) imaging of murine brain tumors at 4 T. Acad Radiol 2001;8:42–47.
18. Grohn OHJ, Lukkarinen JA, Silvennoinen MJ, Pitkanen A, van Zijl PCM, Kauppinen RA. Quantitative magnetic resonance imaging assessment of cerebral ischemia in rat using on-resonance T-1 in the rotating frame. Magn Reson Med 1999;42:268–276.
19. Kettunen MI, Kauppinen RA, Grohn OHJ. Dispersion of cerebral on-resonance T-1 in the rotating frame (T-1ρ) in global ischaemia. Appl Magn Reson 2005;29:89–106.
20. Borthakur A, Gur T, Wheaton AJ, Corbo M, Trojanowski JQ, Lee VMY, Reddy R. In vivo measurement of plaque burden in a mouse model of Alzheimer's disease. J Magn Reson Imaging 2006;24:1011–1017.
21. Michaeli S, Oz G, Sorce DJ, Garwood M, Ugurbil K, Majestic S, Tuite P. Assessment of brain iron and neuronal integrity in patients with Parkinson's disease using novel MRI contrasts. Mov Disord 2007;22: 334–340.
22. Grohn OHJ, Kettunen MI, Makela HI, Penttonen M, Pitkanen A, Lukkarinen JA, Kauppinen RA. Early detection of irreversible cerebral ischemia in the rat using dispersion of the magnetic resonance imaging relaxation time, T-1p. J Cereb Blood Flow Metab 2000;20:1457–1466.
23. Makela HI, Grohn OHJ, Kettunen MI, Kauppinen RA. Proton exchange as a relaxation mechanism for T-1 in the rotating frame in native and immobilized protein solutions. Biochem Biophys Res Commun 2001;289:813–818.
24. Trott O, Palmer AG. R-1 rho relaxation outside of the fast-exchange limit. J Magn Reson 2002;154:157–160.
25. Jin T, Kim S-G. Change of the cerebrospinal fluid volume during brain activation investigated by $T_{1\rho}$-weighted fMRI. Neuroimaging 2010;51:1378–1383.
26. McMahon MT, Gilad AA, Zhou JY, Sun PZ, Bulte JWM, van Zijl PCM. Quantifying exchange rates in chemical exchange saturation transfer agents using the saturation time and saturation power dependencies of the magnetization transfer effect on the magnetic resonance imaging signal (QUEST and QUESP): pH calibration for poly-L-lysine and a starburst dendrimer. Magn Reson Med 2006;55: 836–847.

27. Henkelman RM, Stanisz GJ, Graham SJ. Magnetization transfer in MRI: a review. NMR Biomed 2001;14:57–64.
28. Woessner DE, Zhang SR, Merritt ME, Sherry AD. Numerical solution of the Bloch equations provides insights into the optimum design of PARACEST agents for MRI. Magn Reson Med 2005;53:790–799.
29. Dixon WT, Ren JM, Lubag AJM, Ratnakar J, Vinogradov E, Hancu I, Lenkinski RE, Sherry AD. A concentration-independent method to measure exchange rates in PARACEST agents. Magn Reson Med 2010;63:625–632.
30. Sun PZ. Simultaneous determination of labile proton concentration and exchange rate utilizing optimal RF power: radio frequency power (RFP) dependence of chemical exchange saturation transfer (CEST) MRI. J Magn Reson 2010;202:155–161.
31. Sun PZ, Benner T, Kumar A, Sorensen AG. Investigation of optimizing and translating pH-sensitive pulsed-chemical exchange saturation transfer (CEST) imaging to a 3T clinical scanner. Magn Reson Med 2008;60:834–841.
32. Makela HI, De Vita E, Grohn OHJ, Kettunen MI, Kavec M, Lythgoe M, Garwood M, Ordidge R, Kauppinen RA. B-0 dependence of the on-resonance longitudinal relaxation time in the rotating frame (T-1ρ) in protein phantoms and rat brain in vivo. Magn Reson Med 2004;51:4–8.